RSC Advances

ROYAL SOCIETY
OF CHEMISTRY

PAPER

View Article Online
View Journal | View Issue

Check for updates

Cite this: *RSC Adv.*, 2026, **16**, 24272

High-performance 2D $MoTe_2$-based photodetectors with superior Vis-NIR detection capability

Xin Wang, *[abc] Qingyu Zhou,[d] Junkai Shen,[d] Lin Lin,[b] Hailing Tu*[ac]
and Guohu Zhang*[abc]

Received 10th January 2026
Accepted 27th April 2026

DOI: 10.1039/d6ra00257a

rsc.li/rsc-advances

Photodetectors are crucial components for photoelectric conversion in intelligent sensing applications, and their performance can be significantly enhanced by using two-dimensional (2D) materials. In this study, we present a detailed investigation of 2H-$MoTe_2$-based field-effect transistors (FETs) for photodetection. We demonstrate that air annealing at specific temperatures effectively improves charge transport properties by stabilizing the electrical polarity, enhancing transconductance by 230% and carrier mobility by 41%, primarily through defect healing in the $MoTe_2$ lattice. The optimized 2D $MoTe_2$ photodetector exhibits an impressive responsivity of 3.53 A W^{-1} and an external quantum efficiency (EQE) of 652% at 808 nm under 0.08 mW mm^{-2}. Furthermore, the constructed $MoTe_2/MoSe_2$ van der Waals heterojunction exhibits excellent rectifying behavior and ultralow dark current ($<10^{-13}$ A at $V_{gs} = -30$ V). It delivers a peak responsivity of 3.32 A W^{-1} at 671 nm, with an EQE of 614% and a photocurrent-to-dark-current ratio of 466 under 0.009 mW mm^{-2}. These results highlight the potential of 2D materials, particularly $MoTe_2$ and its heterojunctions, for high-performance visible-to-near-infrared(Vis-NIR) photodetection, paving the way for advanced applications in optoelectronics.

1. Introduction

Photodetectors, as the core components for photoelectric signal conversion, play a crucial role in information acquisition in intelligent sensing systems.[1] With the rapid advancement of modern information technologies, there is a growing demand for photodetectors with nanosecond-level response, micron-scale dimensions, high quantum efficiency, multispectral compatibility, and cost-effective large-scale integration.[2–5] However, traditional photodetectors are constrained by their narrowband response and complex fabrication processes, falling short of meeting these emerging requirements.[1,6] The development of next-generation photodetectors is therefore imperative.

Two-dimensional (2D) materials, owing to their dimensional advantages, exhibit superior performance in fabrication, integration, and stability, showing broad application prospects in optoelectronic devices, spintronics, and energy catalysis.[7–12] When material thickness is reduced to the atomic scale, significantly enhanced quantum confinement effects can impart novel physical properties.[13] Among these, Group VI transition metal tellurides (TMTs) have attracted considerable attention due to their unique electronic structures and exotic quantum phenomena. These materials, with the general formula MTe_2 ($M = Cr, Mo, W$), can crystallize in various phases such as 2H, 1 T′, and Td. This structural diversity makes them ideal platforms for exploring exotic quantum states, including the quantum spin Hall effect,[14,15] topological superconductivity,[16] anisotropic spin–orbit coupling,[17] and Weyl semimetal states.[18,19] Within this family, two-dimensional molybdenum telluride ($MoTe_2$) stands out as a representative material.

As a recent addition to the monolayer semiconductor family of transition metal dichalcogenides (TMDCs),[20] $MoTe_2$ has emerged as a focal material for optoelectronic research due to its exceptional photoresponse characteristics. Experimental studies have demonstrated its superior room-temperature mobility (>100 cm^2 V^{-1} s^{-1}),[21] addressing the performance limitations of conventional n-type 2D materials, such as MoS_2.[22] Monolayer $MoTe_2$ is a direct-bandgap semiconductor with a bandgap of $\sim$1.1 eV,[23] comparable to crystalline silicon, and has an interlayer spacing of about 0.7 nm[24] with semimetallic characteristics.[25,26]

Significant progress has been made in $MoTe_2$-based photodetectors. For instance, Huang *et al.*[27] developed a $MoTe_2$ photodetector that demonstrated broadband response across the 0.6–1.55 μm range, achieving a responsivity of 24 mA W^{-1} at

---

[a] *GRINM National Engineering Research Center for Key Materials of Integrated Circuits, Beijing 100088, China. E-mail: wangxin@gritek.com; tuhl@grinm.com; zhangguohu@gritek.com*

[b] *GRINM Semiconductor Materials Co., Ltd, Beijing 100088, China*

[c] *General Research Institute for Nonferrous Metals, Beijing 100088, China*

[d] *School of Materials Science and Engineering, University of Science and Technology Beijing, Beijing 100083, China*

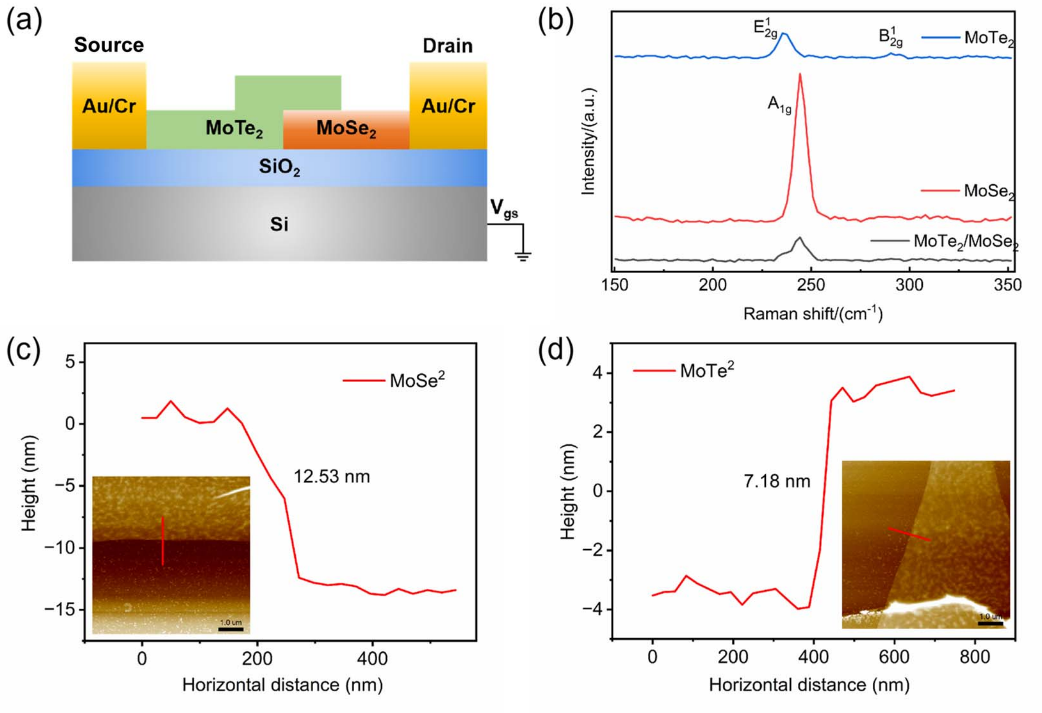

Fig. 1 Structure and characteristics of $MoTe_2/MoSe_2$ heterojunction. (a) Structure of $MoTe_2/MoSe_2$ heterojunction device. (b) Raman mapping of $MoTe_2/MoSe_2$ heterojunction. (c) The thickness of $MoSe_2$.Inset:the AFM image of $MoSe_2$. (d) The thickness of $MoTe_2$. Inset: the AFM image of $MoTe_2$.

1060 nm. Luo *et al.*[28] engineered a vertical $MoTe_2/MoSe_2$ heterojunction photodetector with exceptional performance, achieving a photocurrent-to-dark-current ratio greater than 10^4 under white light and a responsivity of 1.5 A W^{-1}. Chen's team[29] utilized chemical vapor deposition (CVD) to fabricate $MoTe_2/MoS_2$ heterostructures, attaining microsecond-scale response times ($\tau < 5$ μs) with wavelength- and power-dependent photoresponse dynamics. Notably, Hu *et al.*[30] realized a self-powered $MoTe_2/MoSe_2$ photodetector, achieving 0.72 A W^{-1} responsivity, 41.3% external quantum efficiency (EQE), and 7×10^{11} Jones detectivity at 638 nm, coupled with a rapid 120 μs response. This breakthrough provides critical material support for developing all-2D CMOS integrated circuits, aligning with emerging demands for low-power logic architectures and high-efficiency photo-electric conversion systems.

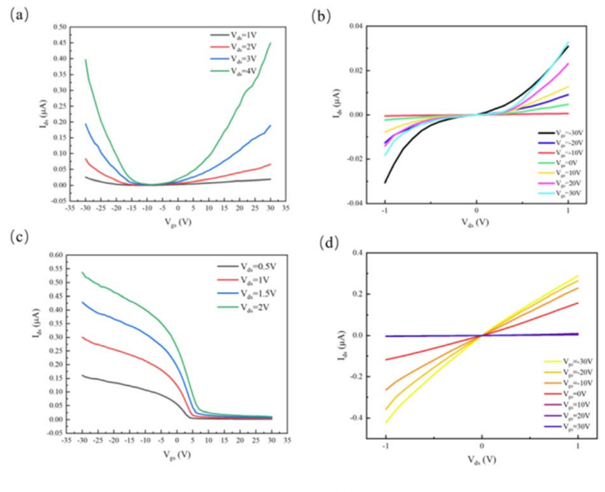

Fig. 2 Electrical properties of $MoTe_2$. (a) Pre-annealing transfer curve. (b) Pre-annealing output curve. (c) Post-annealing transfer curve. (d) Post-annealing output curve.

Despite these advances, key challenges remain for 2D $MoTe_2$ photodetectors. First, achieving an ultralow dark current while maintaining high responsivity and efficiency, particularly in the visible to near-infrared (Vis-NIR) spectrum, is difficult. Second, extending the detection range to cover both Vis and NIR wavelengths without compromising overall performance is nontrivial.

In this work, we address these challenges by optimizing $MoTe_2$-based photodetectors to achieve exceptionally low dark current and broadband detection capability from visible to near-infrared wavelengths. Through air annealing, we significantly improve the transport properties and reduce contact resistance, resulting in highly sensitive photodetectors. Notably, our devices exhibit a record responsivity at 808 nm and an EQE of over 600%, while maintaining ultralow dark current below 10^{-13} A at $V_{gs} = -30$ V. Additionally, the $MoTe_2/MoSe_2$ heterojunctions demonstrate excellent broadband photodetection, with peak responsivity at 671 nm and extended detection to 1064 nm, achieving high specific detectivity.

2. Experimental

2.1 Device fabrication

$MoTe_2$ and $MoSe_2$ flakes were mechanically exfoliated from their bulk crystals using tape (NITTO, 224S) and polydimethylsiloxane

(Gel-Pak, PF). Subsequently, a conventional dry transfer technique was employed to construct the photodetector on a heavily p-doped Si substrate, where the stage was heated to 120 °C and maintained for 3 minutes to release the sample. Two Cr (5 nm)/Au (25 nm) electrodes, connecting to $MoTe_2$ (source) and $MoSe_2$ (drain), were fabricated using a laser direct writer (HWN-LDA-L4), with the Si/SiO_2 substrate serving as a back gate. The channel length of the field-effect transistor is 2.5 μm. Finally, the device was annealed at 210 °C for 15 minutes in ambient air.

2.2 $MoTe_2/MoSe_2$ heterojunction device characterization

The material quality and thickness were characterized using a combination of Raman spectroscopy (Renishaw InVia plus with a 532 nm laser) and atomic force microscopy (AFM, Bruker Multimode 8HR). The Raman spectrum (Fig. 1b) confirms the crystal phase, showing characteristic peaks for 2H-$MoTe_2$ (A_{1g} at 171 cm^{-1} and E_{2g} at 232 cm^{-1}) and $MoSe_2$ (A_{1g} at 242 cm^{-1}). AFM measurements (Fig. 1c and d) reveal film thicknesses of 12.53 nm for $MoSe_2$ and 7.18 nm for $MoTe_2$. Based on the monolayer thickness (~0.8 nm for $MoSe_2$ and 0.7–0.8 nm for $MoTe_2$ (ref. 31 and 32)), these correspond to approximately 15 and 10 layers, respectively, demonstrating precise layer control. For electrical testing, all measurements were conducted on a manual probe station (Lakeshore TTP4) equipped with a vacuum pump, a temperature control system, and a semiconductor characterization system (Tektronix Keithley 4200A-SCS), and all data were obtained at room temperature. Regarding the definitions of response times, the rise time typically refers to the time required for the detector's output current (or voltage) to increase from 10% to 90% of the steady-state dark current upon the onset of the optical signal; correspondingly, the fall time refers to the time period during which the output signal decreases from 90% to 10% of the steady-state photocurrent after the optical signal is turned off.

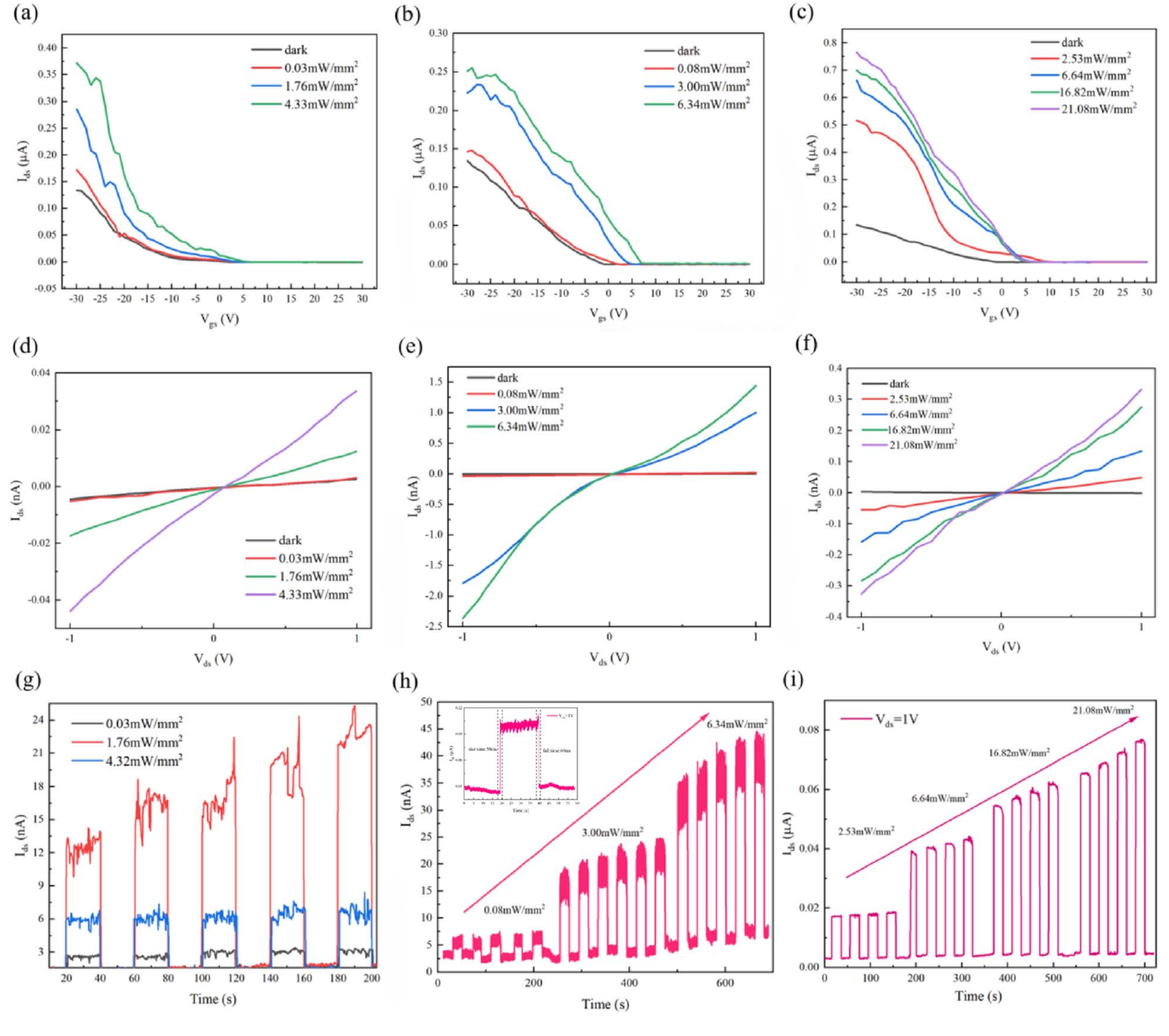

Fig. 3 Optoelectronic properties of $MoTe_2$ photodetector. (a–c) transfer curve under laser wavelength of 671 nm, 808 nm, 1064 nm respectively. (d–f) Output curve under laser wavelength of 671 nm, 808 nm, 1064 nm respectively. (g–i) *I*–*T* curve under laser wavelength of 671 nm, 808 nm, 1064 nm respectively.The inset shows the measured rise and fall times for the pure $MoTe_2$ device under 808 nm laser irradiation.

2.3 Noise analysis and detectivity calculation

The key figures of merit, including photoresponsivity (R_λ), noise equivalent power (NEP), specific detectivity (D^*), and external quantum efficiency (EQE), are calculated using the following formulas:

$$R_\lambda = \frac{I_{\text{ph}}}{P_\lambda S}$$

$$\text{NEP} = \frac{\sqrt{2eI_{\text{dark}}}}{R}$$

$$D^* = \frac{R\sqrt{S}}{\sqrt{2eI_{\text{dark}}}}$$

$$\text{EQE} = \frac{hcR}{e\lambda}$$

where P_λ represents the incident light power density, S and e are the effective area of the lateral homojunction and the unit electric charge, I_{ph} is the current value measured under illumination and I_{dark} is the dark current, h is the Planck constant, and c is the speed of light.

3. Results and discussion

3.1 MoTe$_2$ FET

Electrical characterization of thin 2D MoTe$_2$ devices revealed bipolar transport behavior, with dual conduction thresholds observed in the transfer curves under gate voltage sweeps (from −30 V to 30 V) (Fig. 2a). Enhanced nonlinearity in the output curves further confirmed the presence of Schottky contacts at the Cr/MoTe$_2$ interfaces (Fig. 2b). A 15 minutes air annealing treatment at 210 °C induced transformative changes. Specifically, the Cr/MoTe$_2$ contact transitioned from Schottky to ohmic behavior, with an 85% reduction in contact resistance, while the carrier polarity switched reversibly from n-type to p-type. This was accompanied by a 3.2× increase in hole mobility (from 14.3 cm^2 V^{-1} s^{-1} to 46 cm^2 V^{-1} s^{-1}) (Fig. 2c and d).

This phenomenon is attributed to oxygen-mediated Te vacancy passivation, which reduced the free electron density (from 10^{17} to 10^{15} cm^{-3}) and modulated Schottky barriers: the electron barrier increased by 0.14 eV, while the hole barrier decreased by 0.12 eV. Notably, thick MoTe$_2$ films (35.8 nm), which initially exhibited n-type Schottky-limited transport, also achieved p-type conversion post-annealing, despite a weakened quantum confinement effect. This demonstrates the universality of the oxygen-intercalation mechanism in controlling the carrier polarity of MoTe$_2$.

Stable p-type operation persisted across a wide range of bias voltages ($-30\text{ V} \leq V_{\text{gs}} \leq 30\text{ V}$, $1\text{ V} \leq V_{\text{ds}} \leq 3\text{ V}$), confirming that air annealing is a robust and effective strategy for contact engineering and polarity control in 2D semiconductors.[33–35] This approach addresses the Fermi-level pinning challenges in transition metal dichalcogenide (TMD) electronics, offering a practical route for enhancing device performance and enabling more versatile applications in optoelectronic and electronic systems.

3.2 MoTe$_2$ photodetector

Photoresponse characterization across the 671–1064 nm spectral range demonstrated wavelength-optimized performance in MoTe$_2$ photodetectors. The p-type transport was significantly enhanced under a −30 V gate bias as the light intensity increased.

At 671 nm, the device exhibited well-balanced optoelectronic characteristics, achieving peak performance at 808 nm with a record responsivity of 3.53 A W^{-1}, ultrawide noise equivalent power (NEP) of 8.20×10^{-15} W Hz$^{-1/2}$, and exceptional EQE of

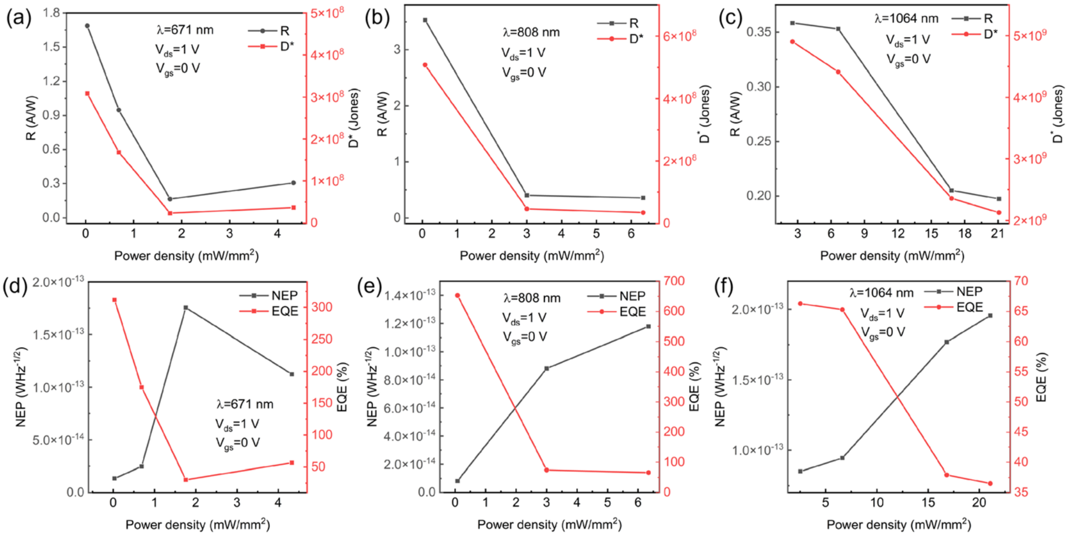

Fig. 4 MoTe$_2$ photodetector. (a–c) R and D under 671 nm, 808 nm, 1064 nm laser respectively. (d–f) NEP and EQE under 671 nm, 808 nm, 1064 nm laser respectively.

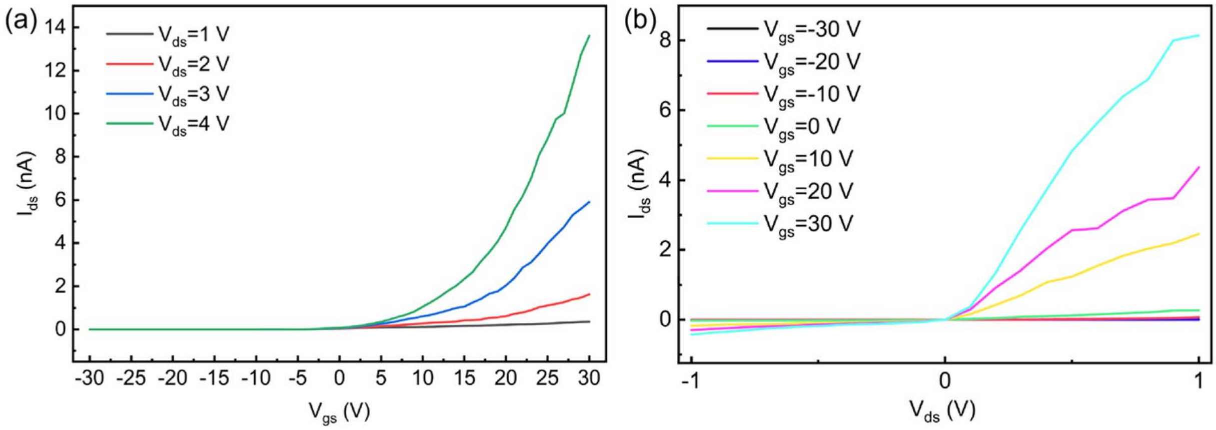

Fig. 5 Electrical properties of $MoTe_2/MoSe_2$ heterojunction. (a) Transfer curve. (b) Output curve.

652%. The rise/fall times of the pure $MoTe_2$ device is approximately 58 ms and 60 ms under 808 nm laser irradiation, respectively. Extension of operation to 1064 nm revealed a strong weak-signal detection capability, evidenced by a maximum photocurrent-to-dark-current ratio of 17.67 and a specific detectivity of 4.90×10^9 Jones in Fig. 3 and 4.

Notably, an inverse correlation was observed between illumination intensity and key metrics: responsivity decreased by 68%, and detectivity dropped by 74% across the 0.01–1 mW mm^{-2} range. This behavior is attributed to trap-state saturation dynamics in the 2D system. Under low-intensity conditions, trap-mediated carrier lifetime enhancement ($\tau\uparrow$) led to photoconductive gain ($G\uparrow$), resulting in increased responsivity ($R \propto G$). However, at high intensities, the saturation of trap states reduced charge separation efficiency and increased recombination losses, causing a decrease in both responsivity and detectivity. This intensity-dependent quantum efficiency degradation,[36–38] coupled with emerging thermal noise, establishes fundamental limits for gain optimization in low-dimensional photodetectors. These findings provide critical insights into trap-state engineering for advanced optoelectronic systems, informing future strategies for improving device performance. Besides, $MoTe_2$-based photodetectors demonstrate considerable long-term stability and cyclic durability, a critical feature for practical applications.[39,40]

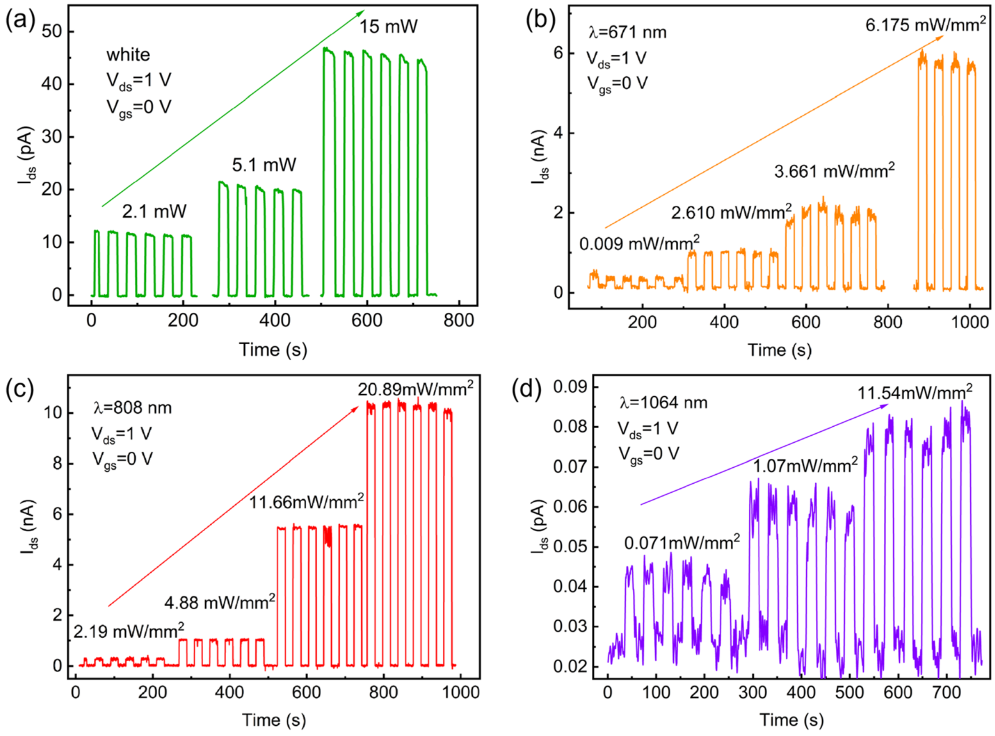

Fig. 6 *I–T* curve of $MoTe_2/MoSe_2$ heterojunction photodetector. (a) White. (b) 671 nm. (c) 808 nm. (d) 1064 nm.

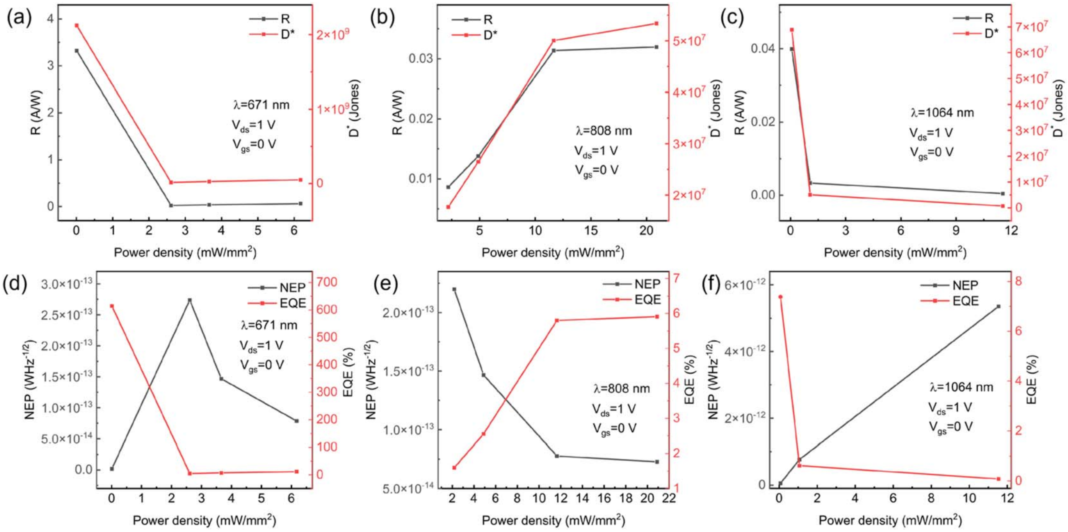

Fig. 7 $MoTe_2/MoSe_2$ heterojunction photodetector. (a–c) R and D under 671 nm, 808 nm, 1064 nm laser respectively. (d–f) NEP and EQE under 671 nm, 808 nm, 1064 nm laser respectively.

3.3 $MoTe_2/MoSe_2$ heterojunction photodetector

Electrical characterization of the $MoTe_2/MoSe_2$ heterojunction revealed n-type conductivity in the dark-state transfer curves (Fig. 5), with pronounced rectification behavior (rectification ratio = 23 at $V_{ds} = \pm 1$ V, $V_{gs} = 0$ V). This rectification arises from the type-II band alignment: the conduction band minimum (CBM) of $MoTe_2$ (~3.8 eV) and $MoSe_2$ (~4.1 eV) forms an interfacial built-in electric field, driving electron transfer from $MoSe_2$ to $MoTe_2$ and hole migration in the reverse direction under equilibrium conditions.

This charge redistribution results in upward band bending at the $MoSe_2$ interface (electron depletion) and downward band bending at $MoTe_2$ (hole depletion),[41] establishing a voltage-dependent barrier modulation mechanism—forward bias reduces the interlayer barrier for electron transport, while reverse bias enhances it.

The photoresponse evaluation across the visible to near-infrared wavelength range, as shown in Fig. 6 and 7, demonstrates broadband detection capabilities, with optimal photodetector performance at a wavelength of 671 nm. At this wavelength, the responsivity reaches 3.32 A W^{-1}, with a quantum efficiency of 614% and an ultralow noise equivalent power (NEP) of 1.83×10^{-15} W $Hz^{-1/2}$ under an optical power density of 0.009 mW mm^{-2}.

The type-II heterostructure enhances carrier separation *via* the built-in electric field,[30,42,43] achieving well-balanced rise/fall times of approximately 31 ms in Fig. 8. Furthermore, extended operation to 808 nm and 1064 nm confirms the spectral versatility of the device. The pure $MoTe_2$ photodetector exhibits slower response (rise/fall times ≈ 58/60 ms) compared to the $MoTe_2/MoSe_2$ heterojunction device. This can be attributed to three main factors. First, the relatively low carrier mobility of pure $MoTe_2$ increases the transit time for photogenerated carriers. Second, higher contact resistance at the metal-$MoTe_2$ interface impedes efficient charge extraction. Finally, the presence of trap states or defects acts as recombination centers, prolonging the carrier lifetime and slowing the current decay. In contrast, the built-in electric field in the heterojunction promotes rapid charge separation and collection, thereby enhancing the response speed. Photodetectors based on thin $MoTe_2$ layers exhibit superior performance metrics—such as higher responsivity, specific detectivity, and faster response times—compared to their thick-layer counterparts. This improvement primarily results from the higher surface-to-volume ratio, better electric field penetration, and enhanced charge transport in thinner layers, which collectively enable more efficient extraction of photogenerated carriers.[44]

However, responsivity and specific detectivity exhibited inverse correlations with light intensity: for instance, R decreased by 68% as light intensity increased from 0.01 to 1 mW mm^{-2}. This is attributed to trap-state saturation: at higher intensities, the increased electron–hole pair density overwhelms the limited trap states, elevating recombination rates and reducing the effective carrier lifetime ($\tau\downarrow$). This leads to a decrease in photoconductive gain ($G\downarrow$) and responsivity ($R \propto G$), while additional shot noise further degrades D^*. As summarized in Table 1, our $MoTe_2$-based heterojunction

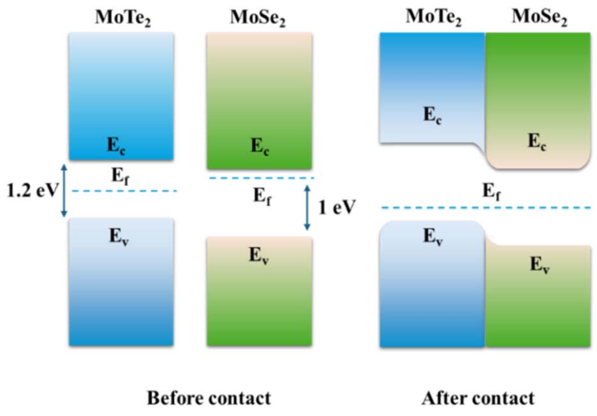

Fig. 8 $MoTe_2/MoSe_2$ heterojunction band diagram.

Table 1 Performance comparison of state-of-the-art $MoTe_2$-based photodetectors

Materials	Light (nm)	R(A/W)	D* (Jones)	EQE	Response time	Ref.
$MoTe_2/SnSe_2$	365	2.05	4.04×10^9	N/A	1.3/4.9 ms	45
$SnSe_2/Bi_2Se_3/MoTe_2$	808	0.493	1.8×10^{11}	76%	553/583 µs	46
$MoTe_2$	520	1.2	4.32×10^8	285%	0.2/0.3 s	44
$MoTe_2/MoSe_2$	638	0.72	7×10^{11}	41%	120/210 µs	30
$MoTe_2/MoSe_2$	White	1.5	2.7×10^{12}	N/A	<30/<35 ms	28
$MoTe_2/MoSe_2$	671	3.32	2.12×10^9	614%	31.2/31.3 ms	This work

photodetector demonstrates a superior overall performance profile—encompassing responsivity, EQE, specific detectivity, response time, and dark current—compared to other reported $MoTe_2$-based devices.[28,30,44–46]

4. Conclusions

In this study, we have demonstrated the substantial enhancement of 2D $MoTe_2$ FETs through air annealing, which significantly improves electrical performance and stability. Air annealing at 210 °C for 15 minutes induced stable p-type conversion, leading to a 7.6-fold increase in transconductance (from 1.84×10^{-9} A V^{-1} to 1.40×10^{-8} A V^{-1}), a 7.6-fold improvement in hole mobility (reaching 4.25 $cm^2 V^{-1} s^{-1}$), and a 5.8-fold boost in carrier density (to 7.83×10^{11} cm^{-2}). These changes were accompanied by a transition from Schottky to ohmic contact, highlighting the significance of defect passivation in enhancing device performance.The optimized $MoTe_2$ photodetector exhibited a peak responsivity of 3.53 A W^{-1} and 652% EQE at 808 nm, with ultralow noise characteristics (8.20×10^{-15} W $Hz^{-1/2}$) under 0.08 mW mm^{-2} illumination, showcasing its potential for high-sensitivity photodetection.

Moreover, the $MoTe_2/MoSe_2$ type-II heterojunction demonstrated broadband detection capabilities, achieving a high responsivity of 3.32 A W^{-1}, an EQE of 614%, and a response time of 31.2 ms at 671 nm. The heterojunction exhibited ultralow dark current ($<10^{-13}$ A) and a rectification ratio of 23, indicating superior electrical characteristics. The 0.3 eV conduction band offset between $MoTe_2$ and $MoSe_2$ generated an efficient built-in electric field, facilitating effective carrier separation and yielding a 466 photocurrent-to-dark-current ratio under 15 mW white light. Notably, the inverse intensity dependence of responsivity (a 68% decrease from 0.01 to 1 mW mm^{-2}) and detectivity were governed by trap-state-limited photoconductive gain, providing crucial insights into the performance limitations and fundamental design constraints of low-dimensional optoelectronic devices.

This work establishes air-annealed 2D $MoTe_2$ as a tunable platform for visible-NIR photodetection and provides valuable guidelines for heterojunction interface engineering, paving the way for the development of next-generation optoelectronic systems with enhanced performance. Further studies on the long-term stability, endurance, and data retention of these devices will be essential to meet the lifetime and reliability requirements for practical applications.

Author contributions

X. W.: conceptualization, investigation (fabrication of devices, Raman spectroscopy, IV measurements), visualization (device diagram drafting), data curation, writing – original draft preparation. Q. Y. Z.: visualization (device diagram drafting), data curation. J. K. S.: conceptualization, investigation (fabrication of devices, A. F. M., Raman spectroscopy, IV measurements), data curation, writing – original draft preparation. L. L.: writing – review & editing. H. L. T.: methodology, supervision. G. H. Z.: methodology, supervision. All authors: validation.

Conflicts of interest

All authors declare no conflicts of interest.

Data availability

Most of the data presented in this paper is included in the main manuscript, and additional data are available from the corresponding author upon reasonable request.

References

1 J. Wang, H. Fang, X. Wang, X. Chen, W. Lu and W. Hu, *Small*, 2017, 13.
2 N. M. Ravindra and V. K. Srivastava, *Infrared Phys.*, 1980, **20**, 399–418.
3 C.-H. Liu, Y.-C. Chang, T. B. Norris and Z. Zhong, *Nat. Nanotechnol.*, 2014, **9**, 273–278.
4 Z. Yang, C. Li, Y. Ran, Y. Li, X. Feng, K. Cui, F. Liu, H. Sun, W. Zhang, Y. Ye, F. Qiao, J. Wang, C.-Z. Ning, C. J. Chang-Hasnain and Y. Huang, *Light: Sci. Appl.*, 2026, **15**, 16.
5 Q.-h. Zhang, Z.-h. Dong, K. Liu, S.-j. Fu, X.-h. Hong, Y.-l. Cao, C. Zhang, J. Du, Y.-q. Lu, Y.-y. Zhu, Y.-f. Chen and X.-j. Zhang, *Nat. Commun.*, 2026, **17**, 2907.
6 S. Zhang, Y. Wu, F. Gao, H. Shang, J. Zhang, Z. Li, Y. Fu and P. Hu, *Adv. Funct. Mater.*, 2022, **32**, 2205299.
7 S. Gao, Z. Wang, H. Wang, F. Meng, P. Wang, S. Chen, Y. Zeng, J. Zhao, H. Hu, R. Cao, Z. Xu, Z. Guo and H. Zhang, *Adv. Mater. Interfaces*, 2020, **8**, 2001730.
8 A. Gao, Z. Zhang, L. Li, B. Zheng, C. Wang, Y. Wang, T. Cao, Y. Wang, S.-J. Liang, F. Miao, Y. Shi and X. Wang, *ACS Nano*, 2019, **14**, 434–441.
9 A. Kuc, N. Zibouche and T. Heine, *Phys. Rev. B*, 2011, **83**, 245213.

10 Y. Zhu, Y. Wang, X. Pang, Y. Jiang, X. Liu, Q. Li, Z. Wang, C. Liu, W. Hu and P. Zhou, *Nat. Commun.*, 2024, **15**, 6015.

11 Z. Qiu, Z. Luo, M. Chen, W. Gao, M. Yang, Y. Xiao, L. Huang, Z. Zheng, J. Yao, Y. Zhao and J. Li, *ACS Nano*, 2024, **18**, 27055–27064.

12 P. Gao, S. Liu, Y. Tang, T. Wang, S. Ran, L. Liu, M. Zhang, F. Tan, J. Chen, J. Wei, X. Zou, Y. Wei, M. Zhong, X. Jiang and J. Wang, *Adv. Funct. Mater.*, 2025, **36**, e14824.

13 S. Tang, C. Zhang, D. Wong, Z. Pedramrazi, H.-Z. Tsai, C. Jia, B. Moritz, M. Claassen, H. Ryu, S. Kahn, J. Jiang, H. Yan, M. Hashimoto, D. Lu, R. G. Moore, C.-C. Hwang, C. Hwang, Z. Hussain, Y. Chen, M. M. Ugeda, Z. Liu, X. Xie, T. P. Devereaux, M. F. Crommie, S.-K. Mo and Z.-X. Shen, *Nat. Phys.*, 2017, **13**, 683–687.

14 S. Wu, V. Fatemi, Q. D. Gibson, K. Watanabe, T. Taniguchi, R. J. Cava and P. Jarillo-Herrero, *Science*, 2018, **359**, 76–79.

15 Y. Qi, P. G. Naumov, M. N. Ali, C. R. Rajamathi, W. Schnelle, O. Barkalov, M. Hanfland, S.-C. Wu, C. Shekhar, Y. Sun, V. Süß, M. Schmidt, U. Schwarz, E. Pippel, P. Werner, R. Hillebrand, T. Förster, E. Kampert, S. Parkin, R. J. Cava, C. Felser, B. Yan and S. A. Medvedev, *Nat. Commun.*, 2016, **7**, 11038.

16 J. Cui, P. Li, J. Zhou, W.-Y. He, X. Huang, J. Yi, J. Fan, Z. Ji, X. Jing, F. Qu, Z. G. Cheng, C. Yang, L. Lu, K. Suenaga, J. Liu, K. T. Law, J. Lin, Z. Liu and G. Liu, *Nat. Commun.*, 2019, **10**, 2044.

17 Z. Wang, D. Gresch, A. A. Soluyanov, W. Xie, S. Kushwaha, X. Dai, M. Troyer, R. J. Cava and B. A. Bernevig, *Phys. Rev. Lett.*, 2016, **117**, 056805.

18 Y. Sun, S.-C. Wu, M. N. Ali, C. Felser and B. Yan, *Phys. Rev. B*, 2015, **92**, 161107.

19 A. A. Soluyanov, D. Gresch, Z. Wang, Q. Wu, M. Troyer, X. Dai and B. A. Bernevig, *Nature*, 2015, **527**, 495–498.

20 W. G. Vandenberghe and M. Rostami Osanloo, *ACS Appl. Electron. Mater.*, 2023, **5**, 623–631.

21 N. R. Pradhan, D. Rhodes, S. Feng, Y. Xin, S. Memaran, B.-H. Moon, H. Terrones, M. Terrones and L. Balicas, *ACS Nano*, 2014, **8**, 5911–5920.

22 Y. F. Lin, Y. Xu, S. T. Wang, S. L. Li, M. Yamamoto, A. Aparecido-Ferreira, W. Li, H. Sun, S. Nakaharai, W. B. Jian, K. Ueno and K. Tsukagoshi, *Adv. Mater.*, 2014, **26**, 3263–3269.

23 C. Ruppert, B. Aslan and T. F. Heinz, *Nano Lett.*, 2014, **14**, 6231–6236.

24 M. Yamamoto, S. T. Wang, M. Ni, Y.-F. Lin, S.-L. Li, S. Aikawa, W.-B. Jian, K. Ueno, K. Wakabayashi and K. Tsukagoshi, *ACS Nano*, 2014, **8**, 3895–3903.

25 D. H. Keum, S. Cho, J. H. Kim, D.-H. Choe, H.-J. Sung, M. Kan, H. Kang, J.-Y. Hwang, S. W. Kim, H. Yang, K. J. Chang and Y. H. Lee, *Nat. Phys.*, 2015, **11**, 482–486.

26 S. Cho, S. Kim, J. H. Kim, J. Zhao, J. Seok, D. H. Keum, J. Baik, D.-H. Choe, K. J. Chang, K. Suenaga, S. W. Kim, Y. H. Lee and H. Yang, *Science*, 2015, **349**, 625–628.

27 H. Huang, J. Wang, W. Hu, L. Liao, P. Wang, X. Wang, F. Gong, Y. Chen, G. Wu, W. Luo, H. Shen, T. Lin, J. Sun, X. Meng, X. Chen and J. Chu, *Nanotechnology*, 2016, **27**, 445201.

28 H. Luo, B. Wang, E. Wang, X. Wang, Y. Sun and K. Liu, *Crystals*, 2019, **9**, 315.

29 Y. Chen, X. Wang, G. Wu, Z. Wang, H. Fang, T. Lin, S. Sun, H. Shen, W. Hu, J. Wang, J. Sun, X. Meng and J. Chu, *Small*, 2018, 14.

30 W. Hu, H. Wang, J. Dong, H. Sun, Y. Wang, Z. Sheng and Z. Zhang, *ACS Appl. Mater. Interfaces*, 2023, **15**, 18182–18190.

31 J.-H. Li, D. Bing, Z.-T. Wu, G.-Q. Wu, J. Bai, R.-X. Du and Z.-Q. Qi, *Chin. Phys. B*, 2020, **29**, 017802.

32 R. Konar and G. D. Nessim, *Mater. Adv.*, 2022, **3**, 4471–4488.

33 Z. Qiu, J. Liao, Y. Zhang, Z. Liu, Z. Wu, H. Zheng, L. Zheng and Y. Zhang, *ACS Appl. Electron. Mater.*, 2025, **7**, 8170–8179.

34 H. Nan, Z. Wang, W. Wang, Z. Liang, Y. Lu, Q. Chen, D. He, P. Tan, F. Miao, X. Wang, J. Wang and Z. Ni, *ACS Nano*, 2014, **8**, 5738–5745.

35 W. Deng, Y. Yu, X. Yan, L. Wang, N. Yu, X. Liao, W. Luo and J. Wu, *ACS Nano*, 2025, **19**, 27526–27537.

36 P. Ma, N. Flöry, Y. Salamin, B. Baeuerle, A. Emboras, A. Josten, T. Taniguchi, K. Watanabe, L. Novotny and J. Leuthold, *ACS Photonics*, 2018, **5**, 1846–1852.

37 H. Fang and W. Hu, *Advanced Science*, 2017, **4**, 1700323.

38 Y. Zou, T. Zou, C. Zhao, B. Wang, J. Xing, Z. Yu, J. Cheng, W. Xin, J. Yang, W. Yu, H. Dong and C. Guo, *Small*, 2020, 16.

39 Y. Wang, S. Wang, Z. Qu, Z. Chen, Y. Zheng, S. Lang, P. Zhang, J. Song, X. Zhang, W. Zhao, F. Yang, J. Lu and H. Liu, *Laser Photon. Rev.*, 2025, **20**, e01819.

40 S. Li, J. Zhou, J. Zhang, S. Yang, J. Xiong, Y. Yang, L. Huang, J. Li and N. Huo, *Wearable Electron.*, 2024, **1**, 281–286.

41 S. Tongay, J. Suh, C. Ataca, W. Fan, A. Luce, J. S. Kang, J. Liu, C. Ko, R. Raghunathanan, J. Zhou, F. Ogletree, J. Li, J. C. Grossman and J. Wu, *Sci. Rep.*, 2013, **3**, 2657.

42 C. Gong, H. Zhang, W. Wang, L. Colombo, R. M. Wallace and K. Cho, *Appl. Phys. Lett.*, 2013, **103**, 053515.

43 S. Liu, Y. Ding, Y. Shi, Y. Feng, R. He, T. Yu, Y. Zheng, S. Li, Z. Zhang, Y. Luo, R. Zhang and J. Chu, *J. Mater. Sci. Technol.*, 2026, **263**, 220–229.

44 S. Hussain, S. Zhao, Q. Zhang and L. Tao, *Nanomaterials*, 2024, **14**, 804.

45 F. Zhang, H. Shi, Y. Yu, S. Liu, D. Liu, X. Zhou, L. Yuan, J. Shi, Q. Xia, Z. Wei, J. He and M. Zhong, *Adv. Opt. Mater.*, 2024, **12**, 2303088.

46 J. Ma, S. Chen, L. Zhao, J. Chen, Z. Lan, M. Yang, Y. Sun, Z. Zheng, W. Gao and J. Li, *Adv. Opt. Mater.*, 2024, **12**, 2302563.